SKPM study on organic-inorganic perovskite materials

Kena Song, Yinghui Wu, Xi Chen, Yi He, Liyu Liu, Guo Chen, and Ruchuan Liu

Citation: AIP Advances **8**, 035114 (2018); doi: 10.1063/1.5021755
View online: https://doi.org/10.1063/1.5021755
View Table of Contents: http://aip.scitation.org/toc/adv/8/3
Published by the American Institute of Physics

SKPM study on organic-inorganic perovskite materials

Kena Song, Yinghui Wu, Xi Chen, Yi He, Liyu Liu, Guo Chen,
and Ruchuan Liu[a]
Department of Physics, Chongqing University, Chongqing 401331, China

(Received 8 January 2018; accepted 7 March 2018; published online 19 March 2018)

We report Atomic Force Microscopy (AFM) and Scanning Kelvin Probe Microscopy (SKPM) studies on the surface morphology and surface potential properties of $CH_3NH_3PbI_3$, $CH_3NH_3PbI_{3-x}Cl_x$, $CH_3NH_3PbI_{3-x}Br_x$ and $CH_3NH_3PbBr_{3-x}Cl_x$, respectively. For $CH_3NH_3PbI_3$ rod structure, its surface potential is independent of the precursor concentration, suggesting a robust electronic feature. Surface potential studies of $CH_3NH_3PbI_3$ particle reveal that the Fermi level within $CH_3NH_3PbI_3$ is strongly influenced by the substrate. In the case of $CH_3NH_3PbI_{3-x}Cl_x$, its surface potential depends on precursor concentrations and we suspect that chlorine concentrated solutions might lead to more chlorine incorporation in the final products, thus lowering its Fermi level. Also, we studied the surface potentials of $CH_3NH_3PbI_{3-x}Br_x$ and $CH_3NH_3PbBr_{3-x}Cl_x$with specified halide ratios. The surface potential differences between different samples are related to their work function variations. These results are helpful to the understanding of the structural and electronic properties of perovskite materials. https://doi.org/10.1063/1.5021755

I. INTRODUCTION

Since their first introduction in solar cells in 2009,[1] methylammonium lead halide perovskite materials (e.g., $CH_3NH_3PbX_3$,X = Cl, Br, I) have attracted much attention in photovoltaic research community.[2–9] The power conversion efficiency of perovskite based solar cells has already surpassed 20% in a few years.[10] Various investigations have revealed their great potential as a prospective candidate for photovoltaic application, featuring with favorable bandgap, high absorption coefficient, high carrier mobility and long electron/hole diffusion length.[11–14]

For iodide/chloride mixed perovskite $CH_3NH_3PbI_{3-x}Cl_x$, a variety of experiments are conducted to investigate the role of chlorine element.[15–25] It shows that Cl ions in the precursor solution have a profound and beneficial effect on the film morphology,[15,16] carrier transport,[13] and stability,[17,26] even though Cl remains at a very low content in the perovskite lattice.[24,25,27,28] For iodide/bromide and chloride/bromide mixed perovskites, their optical and electronic properties can be tuned by changing the halide ratios.[29–31] These perovskites are mostly wide bandgap and are not suitable for photovoltaic applications due to their transparency to most of the solar spectrum. However, recent studies have shown promising prospects for their use in light emission devices whose spectral response can be chemically tuned across the entire visible spectrum.[30,31]

Despite the fast development for perovskite materials, more studies are needed to clearly clarify their structure-property relations. Scanning Kelvin Probe Microscopy (SKPM) is a surface potential detection technique based on AFM. It measures the surface potential or contact potential difference (V_{CPD}) by compensating the electrostatic forces between the microscopic probe and sample. The contact potential difference is generally determined by the effective work function of two materials and the electrostatic potential difference. The former depends on the surface properties of the two materials, and the latter is determined by the bias and surface charges of the sample.[32] SKPM

[a]Email: phyliurc@cqu.edu.cn

is widely used in multiple disciplines to study the morphology and surface electronic properties of materials simultaneously.[33–35] It also has been used for perovskite films to study grain boundary (GB) effects.[36–40] Their SKPM studies revealed a downward band bending in the energy band diagram at the GBs which act as effective charge dissociation interfaces and photocurrent transduction pathways, enhance minority carrier collection and boost the overall performance of the device. However, as SKPM directly gives the local work function/Fermi level of materials, or at least shows the relative energy levels with careful controls on experimental conditions in air, it provides a useful approach to obtain insights on the electronic properties of perovskite and the interaction between perovskite materials and substrates.

In this work, we systematically conduct AFM and SKPM experiments to investigate the morphology and surface potential of $CH_3NH_3PbI_3$, $CH_3NH_3PbI_{3-x}Cl_x$, $CH_3NH_3PbI_{3-x}Br_x$ and $CH_3NH_3PbBr_{3-x}Cl_x$, respectively. For triiodide perovskite, two different structures are formed. The rod structure is made by single-step pre-mixed precursor deposition, particle structure by two-step deposition. The concentration effect and substrate effect on the energy barrier at the perovskite/substrate interfaces are studied. Then by studying $CH_3NH_3PbI_{3-x}Cl_x$ perovskite films deposited from three precursor concentrations, we establish a connection between its Fermi level and chlorine effect. Also, we studied the surface potential of I/Br and Br/Cl mixed perovskites with specified ratios and the surface potential is correlated with their work functions.

II. RESULT AND DISCUSSION

A. Morphology and surface potential study of $CH_3NH_3PbI_3$

We first choose to investigate the most widely studied perovskite $CH_3NH_3PbI_3$.[1] Structures are both formed by solution approaches. The common rod structure is made by one-step pre-mixed precursor deposition, and the particle structure by two-step deposition. Their typical topography images are shown in Figures 1(a) and 1(b), respectively. Four precursor solutions with different concentrations are used to obtain perovskite rods with micrometer-long sizes. Increasing concentration from 4.8 to 29 wt%, the rod length grows from ~4.5 μm to ~20 μm and its average height increases from 5.8 nm to 211.7 nm. For particle perovskite, FTO, PEDOT:PSS/FTO and PEDOT:PSS/glass are used as substrates. The size distributions of obtained rods and particles are summarized in Table I. More topography images can be found in the supplementary material(Figure S1, S4).

Figures 1(g) and 1(h) shows the absorption spectra and PL spectra of both perovskite particles and rods, respectively. Perovskite particles show more pronounced absorption peaks around 420 nm and 500 nm. The absorption spectra of the both structures display a distinct absorption onset around the energy band gap (~760 nm), indicating the formation of perovskite. This is also confirmed by their steady state PL spectra, which show emission peaks around 764 nm. A slight shift in the emission peak (~756 nm) is observed for rod perovskite.

In SKPM measurements, the surface potential is determined by the effective work function of both the probe and sample. For meaningful comparison, a same potential reference is needed. In this section, we choose the substrate potential as reference point as different probes are used in these experiments. To semi-quantitatively discuss this problem, we choose a simple Mott-Schottky (MS) model for inorganic semiconductor/metal contact.[41] Owing to work function difference between the substrate and perovskite semiconductor, electrons are free to move throughout the interface, reaching a thermal equilibrium, leading to Fermi-level alignment and band-bending phenomena at the metal/semiconductor contact.[35] The V_{CPD}, which coincides to the difference of work function between the substrate and the semiconducting solid, reflects an energy barrier that a hole needs to overcome in order to be transferred from perovskite to substrate at the interface.[36,41] The energy level alignment diagram at the $CH_3NH_3PbI_3$/substrate interfaces is depicted in Figure 2.

Typical potential images for rod and particle structures are shown in Figures 1(d) and 1(e), respectively. Quantitative analyses are summarized in Table I. For rod perovskite deposited on n-type FTO substrate, it shows that when precursor concentration is decreased from 29 wt% to 4.8 wt%, the surface potential shows a little variations around 45 meV. There is no obvious

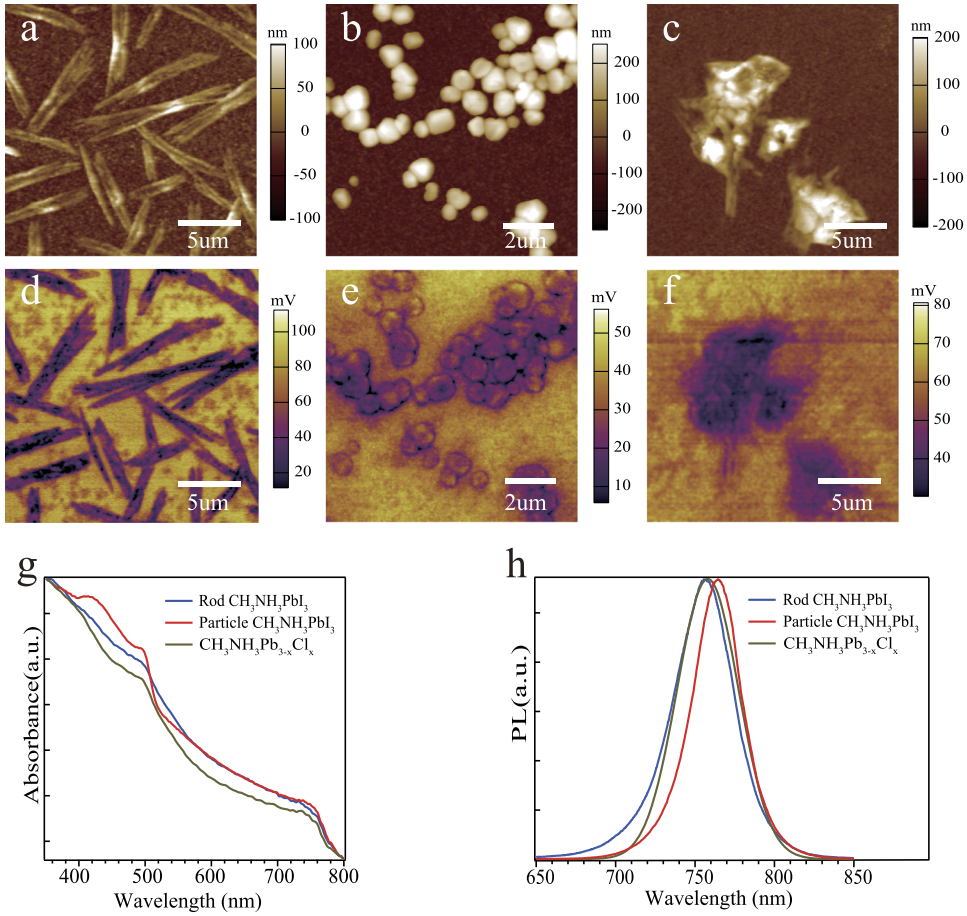

FIG. 1. Topography, surface potential and optical properties of perovskites. (a-c) AFM topography images of rod $CH_3NH_3PbI_3$, particle $CH_3NH_3PbI_3$ and $CH_3NH_3PbI_{3-x}Cl_x$ deposited on FTO substrate, respectively. (d-f) Corresponding contact potential difference obtained by SKPM. (g) Similar absorption spectra both display a distinct absorption onset around 760 nm, indicating the formation of final perovskites. (h) PL spectra of rod $CH_3NH_3PbI_3$ and $CH_3NH_3PbI_{3-x}Cl_x$ share a nearly identical emission peak around 750 nm. A slight shift in the emission peak (~756 nm) is observed for rod $CH_3NH_3PbI_3$.

connections between the surface potential and the rod size. This suggests that the electronic properties of this rod structure perovskite is robust or that $CH_3NH_3PbI_3$ is defect tolerance as small variations in the processing/reaction could lead to an incomplete conversion or structural heterogeneity across the bulk film, resulting defects or different phases in perovskite films. The topography and potential images of these rods made from these precursor solutions are shown in supplementary material (Figure S1, S2, S3).

The surface potential of particle perovskite depends on the substrates used. On the n-type FTO substrate, SKPM measurement exhibits an energy barrier around 11 meV. When another p-type PEDOT:PSS film is spin coated on FTO or glass substrates before the perovskite deposition, the barrier is lowered to around 0 ~4 meV. These results agree with literature which reveals that the Fermi level within $CH_3NH_3PbI_3$ is strongly influenced by the substrate.[42] The n-type substrates (FTO used here) yield strongly n-type surfaces, while the p-type substrates (PEDOT:PSS used here) result in perovskite surfaces that are more p-type like. The small potential difference at perovskite/PEDOT:PSS interface indicates that their Fermi levels are very close before reaching equilibrium as depicted in Figure 2.

B. Morphology and surface potential study of $CH_3NH_3PbI_{3-x}Cl_x$

Iodide/chloride mixed perovskite ($CH_3NH_3PbI_{3-x}Cl_x$) is another widely used perovskite. It possesses the same basic crystalline structure and similar electronic structure as its $CH_3NH_3PbI_3$

TABLE I. Summarized potential of rod $CH_3NH_3PbI_3$, particle $CH_3NH_3PbI_3$ and $CH_3NH_3PbI_{3-x}Cl_x$, together with their height and size distribution.

	Comparison conditions	Surface potential (meV) avg ± std	Height (nm) avg ± std	Size (nm) avg ± std
$CH_3NH_3PbI_3$ rod[a]	29.0 wt%	-45.9 ± 16.8	211.7 ± 137.9	20177.5 ± 6208.4
	21.4 wt%	-36.9 ± 11.9	116.3 ± 202.7	15861.2 ± 3248.5
	6.3 wt%	-51.6 ± 17.0	17.9 ± 16.7	6462.9 ± 2021.1
	4.8 wt%	-45.1 ± 17.3	5.8 ± 11.4	4526.1 ± 1310.8
$CH_3NH_3PbI_3$ Particle[b]	FTO	-11.4 ± 12.3	200.6 ± 49.9	474.8 ± 329.2
	PEDOT/FTO	-4.9 ± 8.5	220.8 ± 25.8	568.6 ± 120.3
	PEDOT/glass	0.0 ± 5.4	107 ± 11.1	400.7 ± 81.1
$CH_3NH_3PbI_{3-x}Cl_x$[c]	32.9 wt%	-174.6 ± 27.7	143.6 ± 144.5	-
	24.7 wt%	-71.4 ± 17.3	100.9 ± 97.4	-
	7.6 wt%	-23.6 ± 9.2	77.8 ± 97.6	-

[a]Precursor solutions with concentrations ranging from 4.8 wt% to 29 wt% are used to form different sized rod $CH_3NH_3PbI_3$.

[b]Particle $CH_3NH_3PbI_3$ is formed on n-type FTO substrate and p-type PEDOT:PSS films, repectively.

[c]The $CH_3NH_3PbI_{3-x}Cl_x$ film is spin coated from precursor solutions with concentrations of 32.9 wt%, 24.7 wt% and 7.6 wt%, respectively.

analogue.[28,43] However, its carrier lifetime and diffusion length are found to increase by more than an order of magnitude.[13] For example, experiment shows that electron-hole diffusion lengths in $CH_3NH_3PbI_{3-x}Cl_x$ exceed 1 μm compared with ~100 nm in $CH_3NH_3PbI_3$. In this section, we study the film morphology and surface potential of $CH_3NH_3PbI_{3-x}Cl_x$ by AFM and SKPM, respectively.

The $CH_3NH_3PbI_{3-x}Cl_x$ films are deposited by spin coating a precursor solution with respective 32.9 wt%, 24.7 wt% and 7.6 wt% concentrations. Its typical topography and surface potential images are compared with $CH_3NH_3PbI_3$ rod in Figure 1. More topography and potential images can be found in supplementary material (Figure S7). Figures 1(g) and 1(h) shows that these two perovskites share nearly identical absorption and PL spectra. However, their topography images are different. Instead of the rod structure made by one-step method for $CH_3NH_3PbI_3$, the structure of $CH_3NH_3PbI_{3-x}Cl_x$ is mainly isolated fused-like crystalline islands with several micrometer in size at least. It is caused by their different crystal growth kinetics. It is reported that the $PbCl_2$ addition affected perovskite crystal formation kinetics by acting as heterogeneous nucleation sites due to its limited solubility in DMF.[44]

The surface potential of $CH_3NH_3PbI_{3-x}Cl_x$ are also different compared with $CH_3NH_3PbI_3$. From the SKPM measurements, its surface potential depends on the concentrations of the precursor used. The surface potential data are summarized in Table I. Its surface potential decreases from 175 meV for 32.9 wt% solution to 71 meV and 24 meV for 24.7 wt% and 7.6 wt% solution, respectively. This indicates that its Fermi level is lowered with the increasing precursor concentrations.

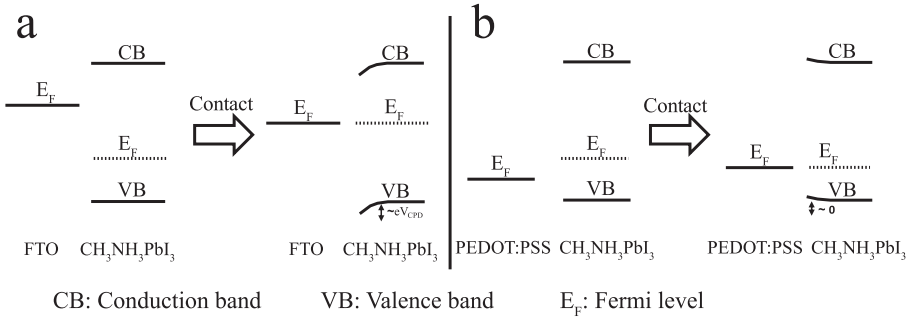

FIG. 2. Energy diagram of $CH_3NH_3PbI_3$ on n-type or p-type substrates before and after contact. (a) N-type substrates (FTO) yield strongly n-type $CH_3NH_3PbI_3$. (b) P-type substrates (PEDOT:PSS) result in p-type like $CH_3NH_3PbI_3$. After contact, electrons are free to move across the interface, leading to Fermi-level alignment and band-bending at the metal/semiconductor contact according to Mott–Schottky model.

By comparing their topography and potential line profiles in Figure S9 in supplementary material, the potential variation is not following its height variation. Thus, the contribution of the substrate to the potential data is neglected.

Here, we speculate that the dependence of surface potential on the precursor concentrations might be related to the presence of chloride in perovskite films. It is expected that more chlorine concentrated solutions might lead to more chlorine incorporation although the content is very low, thus lowering its Fermi level. In a previous study about As-doped CdTe, SKPM experiments revealed that increasing As concentrations in CdTe led to a decrease in V_{CPD}, a downward shift in the CdTe Fermi level and an increase in the CdTe work function.[45] We would expect the same case here. It is also consistent with a recent literature about $CH_3NH_3PbI_3(Cl)$-based perovskite solar cells which found that chlorine incorporation decreased the V_{CPD} compared with $CH_3NH_3PbI_3$, resulting a lower Fermi level.[43] XPS and UPS experiments also confirmed that $CH_3NH_3PbI_{3-x}Cl_x$ has a slight higher work function than $CH_3NH_3PbI_3$.[46] More topography and surface potential can be found in the supplementary material (Figure S7, S8, S9).

C. Morphology and optical properties of I/Br mixed perovskite films

For $CH_3NH_3PbI_{3-x}Cl_x$ perovskite, the chlorine element is believed to be at a very low concentration.[24,25,27,28] It is caused by the limited chloride solubility in the iodide derivative due to the large difference in the ionic radii of ClandI anions.[24] However, for I/Br and Cl/Br mixed perovskites, the composition can be widely tuned from 0 ~1 by varying the halide ratio in the precursor solution.[29–31] Similar conclusions were drawn for other halide compounds, such as $CH_3NH_3SnX_3$,[47] $CH_3NH_3I_{1-x}Br_x$ and $CH_3NH_3Br_{1-x}Cl_x$ (Figure S10 in supplementary material).

I/Br mixed perovskites $CH_3NH_3Pb(I_{1-x}Br_x)_3$ are deposited by spin coating precursors with specified CH_3NH_3I/CH_3NH_3Br ratios mixed with $PbAc_2$ in DMF solvent. As the halide element

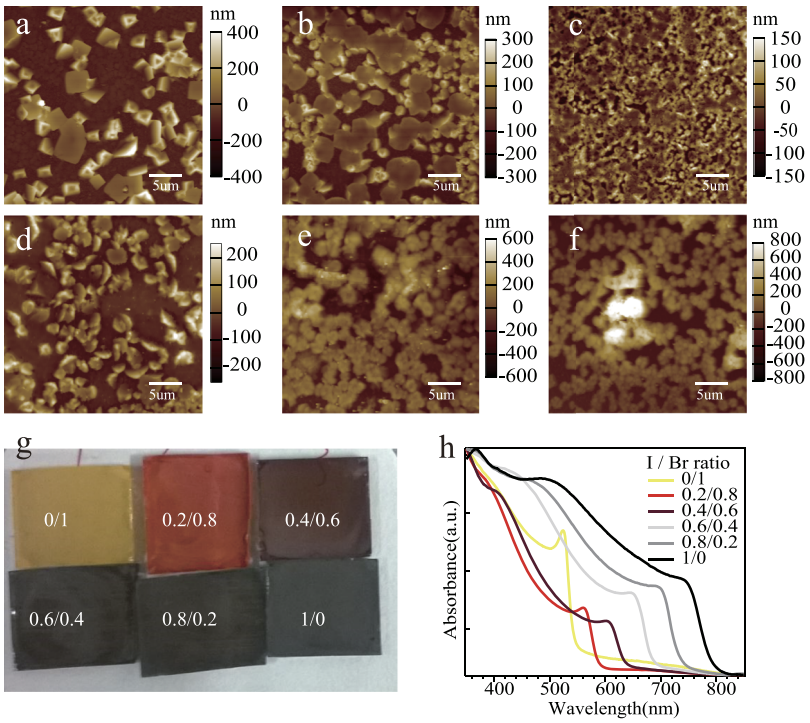

FIG. 3. Topography and optical properties of $CH_3NH_3Pb(I_{1-x}Br_x)_3$ perovskites deposited on FTO substrate. (a-f) AFM topography images of $CH_3NH_3Pb(I_{1-x}Br_x)_3$ spin coated from precursors with CH_3NH_3I/CH_3NH_3Br ratios of 0/1, 0.2/0.8, 0.4/0.6, 0.6/0.4, 0.8/0.2, 1/0, respectively. (g) By tuning the ratio of CH_3NH_3I/CH_3NH_3Br in precursors, the final films change colour from dark brown (1/0) to brown/red (0.8/0.2, 0.6/0.4, 0.4/0.6, 0.2/0.8), then to yellow (0/1) with increasing Br content. (h) Systematic shifting of the absorption edge to shorter wavelength indicates more Br incorporation in the final perovskite films.

comes only from the CH_3NH_3I/CH_3NH_3Br mixtures, Pb source from $PbAc_2$, the final perovskite composition are more easily controlled. Studies also show that the $PbAc_2$ are facilitating the removal of the by-products during crystallization, thus obtaining more continuous films with less pinholes.[48]

Figures 3(a)–3(f) shows topography images of $CH_3NH_3Pb(I_{1-x}Br_x)_3$ on FTO substrate with I/Br ratios of 0/1, 0.2/0.8, 0.4/0.6, 0.6/0.4, 0.8/0.2, 1/0,respectively, for areas of 30 μm*30 μm. It shows a little variation of grain size between different I/Br ratio mixed perovskite. The 0.4/0.6 ratio film has a more compact structure than the other ratio films which have less connections between grains. The 0/1 and 0.2/0.8 ratio films both consisted by more separated grains. And the 0.8/0.2, 1/0 ratio film have a very similar network structure. One thing to note is that the voids between grains may be also covered by the perovskite materials as the void surface is different from the bare FTO substrate.

Figures 3(g) and 3(h) shows the corresponding photographs and absorption spectra of $CH_3NH_3Pb(I_{1-x}Br_x)_3$ with specified I/Br ratios respectively. Through the ratio control of CH_3NH_3I/CH_3NH_3Br, the film colors are tuned from dark brown for $CH_3NH_3PbI_3$ (ratio I/Br=1/0) to brown/red (0.8/0.2, 0.6/0.4, 0.4/0.6, 0.2/0.8 ratios) and then to yellow for $CH_3NH_3PbBr_3$(I/Br=0/1)

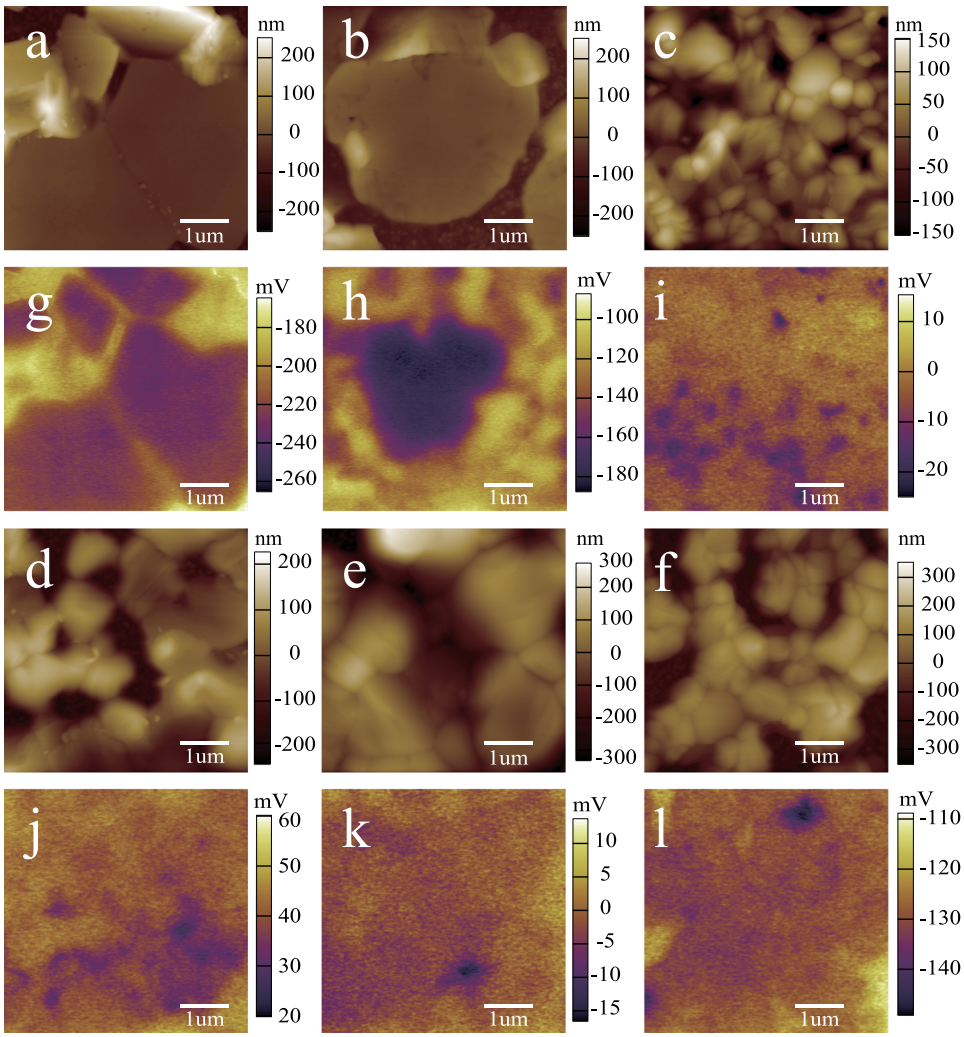

FIG. 4. SKPM results of $CH_3NH_3Pb(I_{1-x}Br_x)_3$ perovskites deposited on FTO substrate for an area of $5^*5\mu m^2$. (a-f) AFM surface topography and (g-l) Corresponding surface potential maps of $CH_3NH_3Pb(I_{1-x}Br_x)_3$ with CH_3NH_3I/CH_3NH_3Br ratio of 0/1, 0.2/0.8, 0.4/0.6, 0.6/0.4, 0.8/0.2, 1/0 used in precursors, respectively.

TABLE II. Average potential of $CH_3NH_3Pb(I_{1-x}Br_x)_3$ perovskites for an area of 5μm*5μm with indicated CH_3NH_3I/CH_3NH_3Br ratio used in precursor solutions. The standard deviation (STD) reflects the local work function inhomogeneities.

Sample number	CH_3NH_3I/CH_3NH_3Br ratio	Surface potential (meV)	STD
1	0/1	-172	40.6
2	0.2/0.8	-135	35.9
3	0.4/0.6	-61	7.9
4	0.6/0.4	31	3.2
5	0.8/0.2	-2	2.9
6	1/0	-123	3.6

with increasing Br content. A systematic shift of the absorption band edge to shorter wavelength with increasing Br content in $CH_3NH_3Pb(I_{1-x}Br_x)_3$ indicates the incorporation of Br element, resulting in the energy band gap (Eg) changes. Also notes that samples with higher Br content (ratio 0/1 and 0.2/0.8) exhibit a peak at the absorption edge that is related to an excitonic transition that appears due to the higher exciton binding energy at high Br concentration.[49]

D. Surface potential study of I/Br mixed perovskite films

Figure 4 shows the enlarged surface topography and the corresponding surface potential maps of perovskite films with I/Br ratio of 0/1, 0.2/0.8, 0.4/0.6, 0.6/0.4, 0.8/0.2, 1/0, respectively for areas of 5 μm*5 μm. As the same probe is used for this group of samples, the surface potential can be directly compared. In this case, the V_{CPD} is defined as the effective work function difference between the tip and sample. The average surface potential of different I/Br ratios mixed films are summarized in Table II. The potential increases from -172 meV for $CH_3NH_3PbBr_3$(I/Br=0/1) to 31 meV (I/Br=0.6/0.4). Further increasing the I/Br ratio to 1/0, however, the potential decreases to -123 meV. The surface potential of $CH_3NH_3Pb(Br_{1-x}Cl_x)_3$ with Cl/Br ratios of 0/1, 0.2/0.8, 0.4/0.6, 0.6/0.4, 0.8/0.2, 1/0, are also studied here. The corresponding AFM topography and SKPM surface potential images, along with their optical absorption spectra are shown in the supplementary material (Figure S11, S12, S13, S14). Their potential data are summarized in Figure 5. The work functions of $CH_3NH_3Pb(Br_{1-x}Cl_x)_3$ from literature decreases first and then increases, with increasing the ratio of Cl/Br.[50] Similar trend is seen in the average potential of $CH_3NH_3Pb(Br_{1-x}Cl_x)_3$ while quite large fluctuations also exist. As in amplitude modulation SKPM, both the tip apex and the cantilever would contribute to the measured V_{CPD}.[51] Also, the experiments are conducted in ambient conditions.

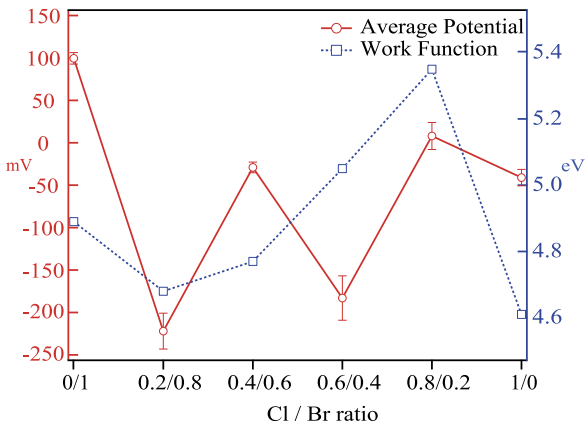

FIG. 5. Average potential of $CH_3NH_3Pb(Br_{1-x}Cl_x)_3$ with specified CH_3NH_3Cl/CH_3NH_3Br ratio (0/1, 0.2/0.8, 0.4/0.6, 0.6/0.4, 0.8/0.2, 1/0) used in precursor solutions. It shows a trend of a fall at a low ratio of Cl/Br followed by a rise when the ratio of Cl/Br is around 4, similar to the trend in the work function.[50] Reproduced with permission from Comin *et al.*, Journal of Materials Chemistry C **3**, 8839–8843 (2015). Copyright 2015 The Royal Society of Chemistry.

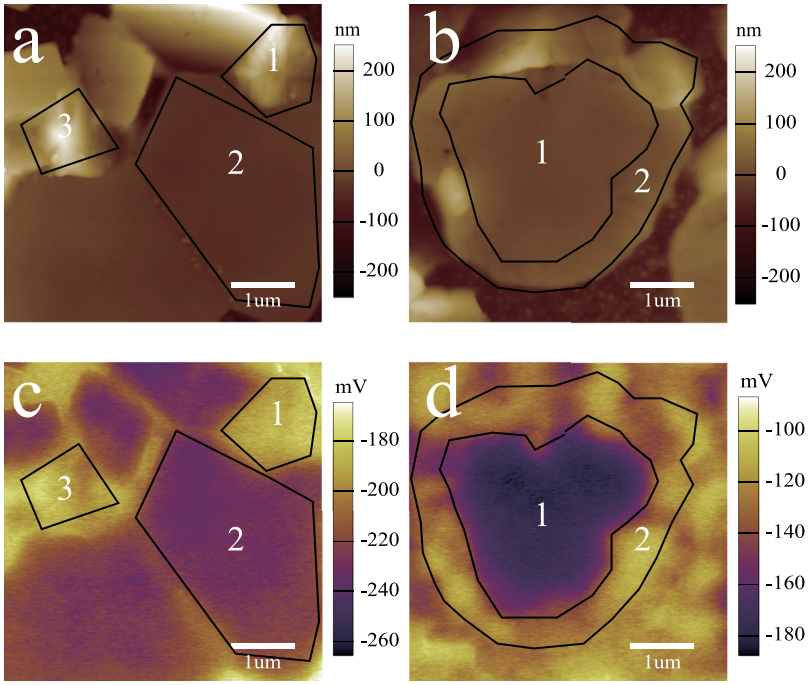

FIG. 6. Local surface potential variations of $CH_3NH_3Pb(I_{1-x}Br_x)_3$. (a-b) Local topography and (c-d) potential images of I/Br mixed perovskites with CH_3NH_3I/CH_3NH_3Br ratio of 0/1 and 0.2/0.8, respectively. The work function variations of different grains are highlighted with boxes.

Thus, the measured V_{CPD} differences among samples do not fully correspond to their work function differences.[52,53]

Not only the average work function can be obtained from the SKPM measurements, the local inhomogeneities in materials can also be analysed from its potential images. For $CH_3NH_3Pb(I_{1-x}Br_x)_3$, work function variations appear for both samples and are most pronounced in 0/1 and 0.2/0.8 mixed films. They are highlighted in the potential images in Figure 6. In the 0/1 ratio mixed perovskite, area 1 and area 3 with similar potentials both appear on the grain boundary. The potential difference between area 1 (about -190 meV) and area 2 (about -227 meV) is 37 meV. These grain-to-grain variations appear to depend on the physical orientation of each grain and its associated crystallographic face. In 0.2/0.8 ratio mixed perovskite, the interior grain area 1 (about -172 meV) has a lower potential than edge area 2 (about -133 meV) and the potential difference is 40 meV. Regarding the reasons of these local work function shift, it might be attributed to local contaminants, such as chemisorbed or physisorbed H_2O molecules, solvent residues etc., resulting in a decrease of the local vacuum energy and the electron affinity.[54] However, as the experiments are conducted in similar conditions and the inhomogeneities are most pronounced in 0/1 and 0.2/0.8 mixed films, we believe that the variations are most likely attributed to compositional inhomogeneities. Previous studies show that for I/Br mixed halide systems, there is compositional inhomogeneity.[55]

III. CONCLUSION

In summary, we have studied the morphology and surface potential of tri-iodine perovskite, I/Br mixed perovskite and Br/Cl mixed perovskite, respectively. For tri-iodide perovskite, two different structures are formed. The SKPM measurement reveals that the energy barrier at rod/FTO interface is independent of the precursor concentrations used. The potential of particle perovskite is directly correlated with the type of substrate used. The n-type FTO substrate yield an n-type surface, while the p-type PEDOT:PSS film results in perovskite surfaces that are more p-type with a lower energy

barrier. For chloride mixed perovskite, measurements show the energy barrier is decreased from 175 meV to 71 meV and 24 meV for 32.9 wt%, 24.7 wt% and 7.6 wt%, respectively. It is expected that chlorine concentrated solutions might lead to more chlorine incorporation, thus lowering its Fermi level. Also, we studied the surface potential of I/Br and Br/Cl mixed perovskites with specified ratios. The surface potential trend between samples is directly related to their work functions. We believe these studies are helpful to understand the structural, optical and electronic properties of perovskite materials.

IV. EXPERIMENTAL

A. Materials

All the chemicals were purchased from Aladdin Inc unless specified and were used as received without further purification, including HI (55-58 wt% in water), HBr(ACS, 48 wt%), HCl(36-38%), CH_3NH_2(AR, 30-33 wt% in absolute ethanol), PbI_2(99.9% metals basis),$PbCl_2$(99.99% metals basis), $Pb(Ac)_2 \cdot {}_3H_2O$ (99.99% metals basis), N,N-dimethylformamide (GC, > 99.9%), Isopropyl Alcohol (AR, ≥ 99.5%), diethyl ether (AR), ethanol (ACS, ≥ 99.5%), acetone (AR). PEDOT:PSS (Clevios PH 1000) was purchased from H.C.Starck.

1. Methylammonium halide synthesis

Methylammonium halide (CH_3NH_3I,CH_3NH_3Br,CH_3NH_3Cl) was synthesized by the reaction of methylamine aqueous solution and the corresponding hydrohalide (HCl,HBr,HI) acid in a beaker at room temperature for 2 h with constant stirring. The precipitate was recovered by carefully evaporating the solvents at 70 °C. The raw product CH_3NH_3X was then rinsed with diethyl ether and dried at 60 °C in a vacuum oven overnight.

Methylammonium mix halides ($CH_3NH_3I_{1-x}Br_x$ and $CH_3NH_3I_{1-x}Cl_x$) were synthesized by evaporating the specified ratio of CH_3NH_3I(CH_3NH_3Cl) and CH_3NH_3Br in ethanol solution at 70 °C. The raw product was rinsed with diethyl ether and dried at 60 °C in a vacuum oven overnight.

B. Precursor preparation and film formation

Before the film deposition, FTO coated glass substrates and glass substrates were cleaned with DI water, acetone and ethanol, for 10 min successively in ultra sonicator. Then the substrates were rinsed by DI water and dried with clean air.

To deposit tri-iodide perovskite rod, CH_3NH_3I powder and PbI_2 were dissolved in DMF at 1: 1 molar ratio with required concentrations. The obtained solution was stirred overnight before use. Then the precursor was spin coated on FTO substrate at the rotation speed of 3000 rpm for 40 s. The film was finally annealed at 100 °C for 30 min on the hotplate.

To deposit tri-iodide perovskite particle, CH_3NH_3I powder and PbI_2 were dissolved in IPA and DMF with a concentration of 30 mg/ml and 100 mg/ml, respectively. For FTO substrate based sample, hot PbI_2 precursor solution (70 °C) was directly spin coated on FTO surface at a rotation speed of 2000 rpm for 40 s without further annealing. For PEDOT:PSS/FTO or PEDOT:PSS/glass substrate based samples, PEDOT:PSS solution was first spin coated on the FTO or glass substrate at a rotation speed of 2000 rpm for 40 s, followed by annealing at 130 °C for 15 min. Then the hot PbI_2 precursor solution (70 °C) was spin coated on the PEDOT:PSS surface at a rotation speed of 2000 rpm for 40 s. After that, the prepared CH_3NH_3I solutions were spin coated on FTO, PEDOT:PSS/FTO and PEDOT:PSS/glass substrates at a rotation speed of 2000 rpm for 40 s. During another spin process, several IPA drops were dripped on the films to clean extra CH_3NH_3I solutions. The obtained films were finally annealed at 100 °C for 30 min.

For chloride mixed perovskite, CH_3NH_3I powder and $PbCl_2$ were dissolved in DMF at 3: 1 molar ratio with required concentrations. The obtained solution was stirred overnight before use. Then the precursor was spin coated on FTO substrate at a rotation speed of 3000 rpm for 40 s. The film was finally annealed at 100 °C for 45 min.

To prepare I/Br and Cl/Br mixed perovskite films, specified CH_3NH_3I(or CH_3NH_3Cl)/CH_3NH_3Br ratios and $PbAc_2$ were dissolved in DMF at 3:1 molar ratio at ~40 wt% concentrations. The obtained

solutions were stirred overnight before use. Then the precursors were spin coated on FTO substrate at a rotation speed of 3000 rpm for 40 s. The films were finally annealed at 100 °C for 10 min.

C. UV-Vis characterization

A UV-3600 spectrophotometer (Shimadzu, Japan) was used for the absorption spectra of samples. PL spectra were recorded by a commercial Micro Raman spectrometer (Horiba), using an excitation laser beam with a wavelength of 532 nm.

D. Morphology and surface potential characterization

SKPM is implemented on an AFM platform (MFP-3D-BIO, Asylum Research). The measurement is carried out in a two-pass technique. The first pass is conducted as a standard AC mode scan and is used to record the surface topography. In the second pass, the tip is then retraced from the first topography scan with an additional z distance of 10 ~50 nm. An AC voltage at a frequency of 60-65 kHz and a tunable DC voltage are applied between the tip and the substrate in the second pass. The DC voltage is adjusted at each point to cancel the force at the AC frequency, and accordingly the value is recorded as the potential difference. In this article, Pt/Cr coated silicon tips (Multi75E-G, Budget sensor) are used. It has an oscillation frequency of 60 kHz, spring constant of 1-5 N/m, and a quality factor Q of ~186. All experiments are conducted in ambient conditions, in dark.

SUPPLEMENTARY MATERIAL

See supplementary material for the detailed data.

ACKNOWLEDGMENTS

This work was supported by the National Natural Science Foundation of China (Grant No. 11474345, No. 11674043).

[1] A. Kojima, K. Teshima, Y. Shirai, and T. Miyasaka, "Organometal halide perovskites as visible-light sensitizers for photovoltaic cells," Journal of the American Chemical Society **131**, 6050–6051 (2009).
[2] J. Im, C. Lee, J. Lee, S. Park, and N. Park, "6.5% efficient perovskite quantum-dot-sensitized solar cell," Nanoscale **3**, 4088–4093 (2011).
[3] H. Kim, C. Lee, J. Im, K. Lee, T. Moehl, A. Marchioro, S. Moon, R. Humphrybaker, J. Yum, J. Moser *et al.*, "Lead iodide perovskite sensitized all-solid-state submicron thin film mesoscopic solar cell with efficiency exceeding 9%," Scientific Reports **2**, 591 (2012).
[4] M. M. Lee, J. Teuscher, T. Miyasaka, T. N. Murakami, and H. J. Snaith, "Efficient hybrid solar cells based on meso-superstructured organometal halide perovskites," Science **338**, 643–647 (2012).
[5] H. Zhou, Q. Chen, G. Li, S. Luo, T. Song, H. Duan, Z. Hong, J. You, Y. Liu, and Y. Yang, "Interface engineering of highly efficient perovskite solar cells," Science **345**, 542–546 (2014).
[6] M. Yang, Y. Zhou, Y. Zeng, C. Jiang, N. P. Padture, and K. Zhu, "Square-centimeter solution-processed planar $CH_3NH_3PbI_3$ perovskite solar cells with efficiency exceeding 15%," Advanced Materials **27**, 6363–6370 (2015).
[7] J. H. Heo, D. H. Song, H. J. Han, S. Y. Kim, J. H. Kim, D. Kim, H. W. Shin, T. K. Ahn, C. Wolf, T. Lee *et al.*, "Planar $CH_3NH_3PbI_3$ perovskite solar cells with constant 17.2% average power conversion efficiency irrespective of the scan rate," Advanced Materials **27**, 3424–3430 (2015).
[8] N. J. Jeon, J. H. Noh, W. S. Yang, Y. C. Kim, S. Ryu, J. Seo, and S. I. Seok, "Compositional engineering of perovskite materials for high-performance solar cells," Nature **517**, 476–480 (2015).
[9] N. Ahn, D. Son, I. Jang, S. M. Kang, M. Choi, and N. Park, "Highly reproducible perovskite solar cells with average efficiency of 18.3% and best efficiency of 19.7% fabricated via Lewis base adduct of lead(II) iodide," Journal of the American Chemical Society **137**, 8696–8699 (2015).
[10] W. S. Yang, J. H. Noh, N. J. Jeon, Y. C. Kim, S. Ryu, J. Seo, and S. I. Seok, "High-performance photovoltaic perovskite layers fabricated through intramolecular exchange," Science **348**, 1234–1237 (2015).
[11] W. Yin, T. Shi, and Y. Yan, "Unique properties of halide perovskites as possible origins of the superior solar cell performance," Advanced Materials **26**, 4653–4658 (2014).
[12] C. Wehrenfennig, G. E. Eperon, M. B. Johnston, H. J. Snaith, and L. M. Herz, "High charge carrier mobilities and lifetimes in organolead trihalide perovskites," Advanced Materials **26**, 1584–1589 (2014).
[13] S. D. Stranks, G. E. Eperon, G. Grancini, C. Menelaou, M. J. P. Alcocer, T. Leijtens, L. M. Herz, A. Petrozza, and H. J. Snaith, "Electron-hole diffusion lengths exceeding 1 micrometer in an organometal trihalide perovskite absorber," Science **342**, 341–344 (2013).
[14] G. Xing, N. Mathews, S. Sun, S. S. Lim, Y. M. Lam, M. Gratzel, S. G. Mhaisalkar, and T. C. Sum, "Long-range balanced electron- and hole-transport lengths in organic-inorganic $CH_3NH_3PbI_3$," Science **342**, 344–347 (2013).
[15] S. T. Williams, F. Zuo, C. Chueh, C. Liao, P. Liang, and A. K. Y. Jen, "Role of chloride in the morphological evolution of organo-lead halide perovskite thin films," ACS Nano **8**, 10640–10654 (2014).

[16] H. Yu, F. Wang, F. Xie, W. Li, J. Chen, and N. Zhao, "The role of chlorine in the formation process of "$CH_3NH_3PbI_{3-x}Cl_x$" perovskite," Advanced Functional Materials **24**, 7102–7108 (2014).
[17] J. Chae, Q. Dong, J. Huang, and A. Centrone, "Chloride incorporation process in $CH_3NH_3PbI_{3-x}Cl_x$ perovskites via nanoscale bandgap maps," Nano Letters **15**, 8114–8121 (2015).
[18] S. Colella, E. Mosconi, G. Pellegrino, A. Alberti, V. L. P. Guerra, S. Masi, A. Listorti, A. Rizzo, G. G. Condorelli, F. De Angelis *et al.*, "Elusive presence of chloride in mixed halide perovskite solar cells," Journal of Physical Chemistry Letters **5**, 3532–3538 (2014).
[19] M. I. Dar, N. Arora, P. Gao, S. Ahmad, M. Gratzel, and M. K. Nazeeruddin, "Investigation regarding the role of chloride in organic–inorganic halide perovskites obtained from chloride containing precursors," Nano Letters **14**, 6991–6996 (2014).
[20] J. Liu and O. V. Prezhdo, "Chlorine doping reduces electron–hole recombination in lead iodide perovskites: Time-domain ab initio analysis," Journal of Physical Chemistry Letters **6**, 4463–4469 (2015).
[21] J. Qing, H. T. Chandran, Y. Cheng, X. Liu, H. Li, S. Tsang, M. Lo, and C. S. Lee, "Chlorine incorporation for enhanced performance of planar perovskite solar cell based on lead acetate precursor," ACS Applied Materials & Interfaces **7**, 23110–23116 (2015).
[22] E. L. Unger, A. R. Bowring, C. J. Tassone, V. L. Pool, A. Goldparker, R. Cheacharoen, K. H. Stone, E. T. Hoke, M. F. Toney, and M. D. Mcgehee, "Chloride in lead chloride-derived organo-metal halides for perovskite-absorber solar cells," Chemistry of Materials **26**, 7158–7165 (2014).
[23] Q. Wang, M. Lyu, M. Zhang, J. H. Yun, H. Chen, and L. Wang, "Transition from the tetragonal to cubic phase of organohalide perovskite: The role of chlorine in crystal formation of $CH_3NH_3PbI_3$ on TiO_2 substrates," Journal of Physical Chemistry Letters **6**, 150929151618007 (2015).
[24] S. Colella, E. Mosconi, P. Fedeli, A. Listorti, F. Gazza, F. Orlandi, P. Ferro, T. Besagni, A. Rizzo, G. Calestani *et al.*, "$MAPbI_{3-x}Cl_x$ mixed halide perovskite for hybrid solar cells: The role of chloride as dopant on the transport and structural properties," Chemistry of Materials **25**, 4613–4618 (2013).
[25] V. L. Pool, A. Goldparker, M. D. Mcgehee, and M. F. Toney, "Chlorine in $PbCl_2$-derived hybrid-perovskite solar absorbers," Chemistry of Materials **27**, 7240–7243 (2015).
[26] Y. Chen, T. Chen, and L. Dai, "Layer-by-layer growth of $CH_3NH_3PbI_{3-x}Cl_x$ for highly efficient planar heterojunction perovskite solar cells," Advanced Materials **27**, 1053–1059 (2015).
[27] G. Grancini, S. Marras, M. Prato, C. Giannini, C. Quarti, F. De Angelis, M. De Bastiani, G. E. Eperon, H. J. Snaith, L. Manna *et al.*, "The impact of the crystallization processes on the structural and optical properties of hybrid perovskite films for photovoltaics," Journal of Physical Chemistry Letters **5**, 3836–3842 (2014).
[28] B. Philippe, B. Park, R. Lindblad, J. Oscarsson, S. Ahmadi, E. M. J. Johansson, and H. Rensmo, "Chemical and electronic structure characterization of lead halide perovskites and stability behavior under different exposures—A photoelectron spectroscopy investigation," Chemistry of Materials **27**, 1720–1731 (2015).
[29] B. Philippe, B. Park, R. Lindblad, J. Oscarsson, S. Ahmadi, E. M. J. Johansson, and H. Rensmo, "Chemical and electronic structure characterization of lead halide perovskites and stability behavior under different exposures—A photoelectron spectroscopy investigation," Chemistry of Materials **27**, 1720–1731 (2015).
[30] N. K. Kumawat, A. Dey, A. Kumar, S. P. Gopinathan, K. L. Narasimhan, and D. Kabra, "Band gap tuning of $CH_3NH_3Pb(Br_{1-x}Cl_x)_3$ hybrid perovskite for blue electroluminescence," ACS Applied Materials & Interfaces **7**, 13119–13124 (2015).
[31] A. Sadhanala, S. Ahmad, B. Zhao, N. Giesbrecht, P. M. Pearce, F. Deschler, R. L. Z. Hoye, K. C. Godel, T. Bein, P. Docampo *et al.*, "Blue-green color tunable solution processable organolead chloride–bromide mixed halide perovskites for optoelectronic applications," Nano Letters **15**, 6095–6101 (2015).
[32] Y. S. Zhou, Y. Liu, G. Zhu, Z. Lin, C. Pan, Q. Jing, and Z. L. Wang, "In situ quantitative study of nanoscale triboelectrification and patterning," Nano Letters **13**, 2771–2776 (2013).
[33] A. Liscio, V. Palermo, and P. Samori, "Nanoscale quantitative measurement of the potential of charged nanostructures by electrostatic and kelvin probe force microscopy: Unraveling electronic processes in complex materials," Accounts of Chemical Research **43**, 541–550 (2010).
[34] W. Melitz, J. Shen, A. C. Kummel, and S. Lee, "Kelvin probe force microscopy and its application," Surface Science Reports **66**, 1–27 (2011).
[35] V. Palermo, M. Palma, and P. Samori, "Electronic characterization of organic thin films by kelvin probe force microscopy," Advanced Materials **18**, 145–164 (2006).
[36] N. Adhikari, A. Dubey, D. Khatiwada, A. F. Mitul, Q. Wang, S. Venkatesan, A. Iefanova, J. Zai, X. Qian, M. Kumar *et al.*, "Interfacial study to suppress charge carrier recombination for high efficiency perovskite solar cells," ACS Applied Materials & Interfaces **7**, 26445–26454 (2015).
[37] Q. Chen, H. Zhou, T. Song, S. Luo, Z. Hong, H. Duan, L. Dou, Y. Liu, and Y. Yang, "Controllable self-induced passivation of hybrid lead iodide perovskites toward high performance solar cells," Nano Letters **14**, 4158–4163 (2014).
[38] G. Y. Kim, S. H. Oh, B. P. Nguyen, W. Jo, B. J. Kim, D. G. Lee, and H. S. Jung, "Efficient carrier separation and intriguing switching of bound charges in inorganic–organic lead halide solar cells," Journal of Physical Chemistry Letters **6**, 2355–2362 (2015).
[39] J. S. Yun, A. Hobaillie, S. Huang, S. H. Woo, Y. Heo, J. Seidel, F. Huang, Y. Cheng, and M. A. Green, "Benefit of grain boundaries in organic–inorganic halide planar perovskite solar cells," Journal of Physical Chemistry Letters **6**, 875–880 (2015).
[40] J. Li, J. Ma, Q. Ge, J. Hu, D. Wang, and L. Wan, "Microscopic investigation of grain boundaries in organolead halide perovskite solar cells," ACS Applied Materials & Interfaces **7**, 28518–28523 (2015).
[41] H. Ishii, N. Hayashi, E. Ito, Y. Washizu, K. Sugi, Y. Kimura, M. Niwano, Y. Ouchi, and K. Seki, "Kelvin probe study of band bending at organic semiconductor/metal interfaces: Examination of fermi level alignment," Physica Status Solidi (A) **201**, 1075–1094 (2004).

[42] E. M. Miller, Y. Zhao, C. C. Mercado, S. K. Saha, J. M. Luther, K. Zhu, V. Stevanović, C. L. Perkins, and d. L. J. Van, "Substrate-controlled band positions in $CH_3NH_3PbI_3$ perovskite films," Physical Chemistry Chemical Physics PCCP **16**, 22122 (2014).
[43] Q. Chen, H. Zhou, Y. Fang, A. Z. Stieg, T. Song, H. Wang, X. Xu, Y. Liu, S. Lu, J. You *et al.*, "The optoelectronic role of chlorine in $CH_3NH_3PbI_3$(Cl)-based perovskite solar cells," Nature Communications **6**, 7269 (2015).
[44] D. T. Moore, H. Sai, K. W. Tan, D. Smilgies, W. Zhang, H. J. Snaith, U. Wiesner, and L. A. Estroff, "Crystallization kinetics of organic-inorganic trihalide perovskites and the role of the lead anion in crystal growth," Journal of the American Chemical Society **137**, 2350–2358 (2015).
[45] W. S. M. Brooks, S. J. C. Irvine, and D. M. Taylor, "Scanning kelvin probe measurements on as-doped CdTe solar cells," Semiconductor Science and Technology **28**, 105024 (2013).
[46] P. Schulz, E. Edri, S. Kirmayer, G. Hodes, D. Cahen, and A. Kahn, "Interface energetics in organo-metal halide perovskite-based photovoltaic cells," Energy and Environmental Science **7**, 1377–1381 (2014).
[47] K. Yamada, K. Nakada, Y. Takeuchi, K. Nawa, and Y. Yamane, "Tunable perovskite semiconductor $CH_3NH_3SnX_3$ (x: Cl, Br, or I) characterized by x-ray and DTA," Bulletin of the Chemical Society of Japan **84**, 926–932 (2011).
[48] W. Zhang, M. Saliba, D. T. Moore, S. Pathak, M. T. Horantner, T. Stergiopoulos, S. D. Stranks, G. E. Eperon, J. A. Alexanderwebber, A. Abate *et al.*, "Ultrasmooth organic–inorganic perovskite thin-film formation and crystallization for efficient planar heterojunction solar cells," Nature Communications **6**, 6142 (2015).
[49] M. Saba, F. Quochi, A. Mura, and G. Bongiovanni, "Excited state properties of hybrid perovskites," Accounts of Chemical Research **49**, 166–173 (2016).
[50] R. Comin, G. Walters, E. S. Thibau, O. Voznyy, Z. Lu, and E. H. Sargent, "Structural, optical, and electronic studies of wide-bandgap lead halide perovskites," Journal of Materials Chemistry C **3**, 8839–8843 (2015).
[51] G. Koley, M. G. Spencer, and H. R. Bhangale, "Cantilever effects on the measurement of electrostatic potentials by scanning kelvin probe microscopy," Applied Physics Letters **79**, 545–547 (2001).
[52] P. Qin, A. L. Domanski, A. K. Chandiran, R. Berger, H. Butt, M. I. Dar, T. Moehl, N. Tetreault, P. Gao, S. Ahmad *et al.*, "Yttrium-substituted nanocrystalline TiO_2 photoanodes for perovskite based heterojunction solar cells," Nanoscale **6**, 1508–1514 (2014).
[53] S. V. Kalinin and D. A. Bonnell, "Local potential and polarization screening on ferroelectric surfaces," Physical Review B **63** (2001).
[54] A. Henning, G. Gunzburger, R. Johr, Y. Rosenwaks, B. Bozicweber, C. E. Housecroft, E. C. Constable, E. Meyer, and T. Glatzel, "Kelvin probe force microscopy of nanocrystalline TiO_2 photoelectrodes," Beilstein Journal of Nanotechnology **4**, 418–428 (2013).
[55] A. Sadhanala, F. Deschler, T. H. Thomas, S. E. Dutton, K. Goedel, F. C. Hanusch, M. L. Lai, U. Steiner, T. Bein, P. Docampo *et al.*, "Preparation of single-phase films of $CH_3NH_3Pb(I_{1-x}Br_x)_3$ with sharp optical band edges," Journal of Physical Chemistry Letters **5**, 2501–2505 (2014).